

Magnetic Phase Diagram of $\text{GdNi}_2\text{B}_2\text{C}$: Two-ion Magnetoelasticity and Anisotropic Exchange Couplings.

M. El Massalami,

*Instituto de Fisica, Universidade Federal do Rio de Janeiro,
CxP 68528, 21945-970 Rio de Janeiro, Brazil*

H. Takeya, K. Hirata,

*National Institute for Materials Science,
1-2-1 Sengen, Tsukuba, Ibaraki, 305-0047, Japan,*

M. Amara, R.-M. Galera and D. Schmitt

*Labo. Magnetisme Louis Neel - CNRS,
BP 166, 38042 Grenoble Cedex 9, France.*

(Dated: November 4, 2018)

arXiv:cond-mat/0302521v1 [cond-mat.mtrl-sci] 25 Feb 2003

Abstract

Extensive magnetization and magnetostriction measurements were carried out on a single crystal of $\text{GdNi}_2\text{B}_2\text{C}$ along the main tetragonal axes. Within the paramagnetic phase, the magnetic and strain susceptibilities revealed a weak anisotropy in the exchange couplings and two-ion tetragonal-preserving α -strain modes. Within the ordered phase, magnetization and magnetostriction revealed a relatively strong orthorhombic distortion mode and rich field-temperature phase diagrams. For $H//(100)$ phase diagram, three field-induced transformations were observed, namely, at: $H_D(T)$, related to the domain alignment; $H_R(T)$, associated with reorientation of the moment towards the c -axis; and $H_S(T)$, defining the saturation process wherein the exchange field is completely counterbalanced. On the other hand, For $H//(001)$ phase diagram, only two field-induced transformations were observed, namely at: $H_R(T)$ and $H_S(T)$. For both phase diagrams, $H_S(T)$ follows the relation $H_S \left[1 - (T/T_N)^2 \right]^{\frac{1}{2}}$ kOe with $H_S(T \rightarrow 0) = 128.5(5)$ kOe and $T_N(H = 0) = 19.5$ K. In contrast, the thermal evolution of $H_R(T)$ along the c -axis (much simpler than along the a -axis) follows the relation $H_R [1 - T/T_R]^{\frac{1}{3}}$ kOe where $H_R(T \rightarrow 0) = 33.5(5)$ kOe and $T_R(H = 0) = 13.5$ K. It is emphasized that the magnetoelastic interaction and the anisotropic exchange coupling are important perturbations and therefore should be explicitly considered if a complete analysis of the magnetic properties of the borocarbides is desired.

PACS numbers: 75.30.Kz, 75.30.Cr, 75.80.+q

I. INTRODUCTION

The field-temperature ($H - T$) magnetic phase diagrams of the intermetallic borocarbides $R\text{Ni}_2\text{B}_2\text{C}$ (R =magnetic rare earth) manifest wide varieties of zero-field magnetic structures such as Neel-type, helimagnetic, amplitude-modulated, and squared-up states.¹⁻⁸ Most of these states, in particular the modulated ones, are unstable against field and temperature variation, leading to a cascade of transformations^{2,3,4} similar to the ones observed in the elemental rare-earths. It is the general opinion that the remarkable features observed in these $H - T$ phase diagrams are governed by the combined influence of exchange couplings and crystalline electric field (CEF) interactions⁹: such an approach reproduced successfully the gross features of the magnetic $H - T$ phase diagrams of $\text{HoNi}_2\text{B}_2\text{C}$. Nevertheless, various experimental observations suggest that two additional interactions, namely, anisotropic exchange interaction and magnetoelastic coupling, are necessary ingredients for the understanding of the behavior of the magnetic borocarbides. Magnetoelastic interactions are spectacularly manifested in the onset of a tetragonal-to-orthorhombic distortion at T_N for $R = \text{Er}, \text{Ho}, \text{Dy}, \text{Tb}$ compounds^{10,11,12,13}, while the anisotropic exchange interactions were reported to be necessary for the description of the low-temperature magnetic properties of $\text{ErNi}_2\text{B}_2\text{C}$ (Ref.¹⁰) and $\text{GdNi}_2\text{B}_2\text{C}$ (Ref.¹⁴). Obviously, the anisotropic exchange interactions and (two-ion) magnetoelastic couplings can be conveniently investigated in $\text{GdNi}_2\text{B}_2\text{C}$ wherein CEF anisotropy is negligible and the de Gennes factor is the strongest.

This work reports a study of the magnetic and magnetoelastic properties of single crystal $\text{GdNi}_2\text{B}_2\text{C}$. The $H - T$ magnetic phase diagrams for fields along the a - and c -axis were determined. Moreover, within the paramagnetic phase, the parastriction and paramagnetic measurements revealed the presence of weakly anisotropic exchange interaction as well as two-ion magnetoelastic couplings while within the ordered state these perturbations were observed to be strong enough to induce a noticeable modification in the nuclear and magnetic structures.

$\text{GdNi}_2\text{B}_2\text{C}$ crystallizes in a body-centered tetragonal structure (space group $I4/mmm$, point symmetry of the Gd site is $4/mmm$).¹⁵ The zero-field magnetic state immediately below $T_N = 19.5$ K is a transverse, incommensurate, sine-modulated structure (moments along b -axis) with a wave vector \vec{k}_a that decreases linearly from $0.551a^*$ at T_N to $0.550a^*$ at $T_R \approx 13.5$ K.^{8,14,16,17,18} At T_R , a moment reorientation sets-in leading to an additional modulated component transversely polarized

along the c -axis.^{8,18} On further temperature decrease, \vec{k}_a increases monotonically reaching $0.553a^*$ at 3.5 K.

II. THEORETICAL BACKGROUNDS

The $7/2S$ -character of $\text{GdNi}_2\text{B}_2\text{C}$ leads to a greater simplification of its magnetic Hamiltonian which is considered to consist mainly of an exchange, a Zeeman, a two-ion magnetoelastic, and an elastic term. Within the mean-field approximation (MFA) the tetragonal-invariant bilinear exchange interaction can be written as a sum of two terms:¹⁹

$$\begin{aligned}\mathcal{H}_{ex}^{\alpha_1} &= -(g_J\mu_B)^2 n^{\alpha_1} \langle J \rangle J, \\ \mathcal{H}_{ex}^{\alpha_2} &= -(g_J\mu_B)^2 n^{\alpha_2} (2 \langle J_z \rangle J_z - \langle J_x \rangle J_x - \langle J_y \rangle J_y)\end{aligned}\quad (1)$$

$\mathcal{H}_{ex}^{\alpha_1}$ corresponds to the isotropic bilinear exchange coupling while $\mathcal{H}_{ex}^{\alpha_2}$ corresponds to an anisotropic bilinear coupling. The values of the isotropic (n^{α_1}) and anisotropic (n^{α_2}) effective exchange coefficients can be determined from the paramagnetic susceptibilities, measured with the field along ($\chi_{\parallel c}$) and perpendicular ($\chi_{\perp c}$) to the c -axis:

$$\begin{aligned}\chi_{\perp c} &= \frac{C}{T - (n^{\alpha_1} - n^{\alpha_2})C} \\ \chi_{\parallel c} &= \frac{C}{T - (n^{\alpha_1} + 2n^{\alpha_2})C}\end{aligned}\quad (2)$$

C is the Curie constant. In Gd-based compounds, the two-ion magnetoelasticity is related to the modification of the magnetic interactions by the strains. For strains that preserve the initial tetragonal symmetry, the two-ion magnetoelastic Hamiltonians can be written as:¹⁹

$$\begin{aligned}\mathcal{H}_{ME}^{\alpha_1} &= -(D_{\alpha_1}^{\alpha_1}\epsilon^{\alpha_1} + D_{\alpha_1}^{\alpha_2}\epsilon^{\alpha_2}) \langle J \rangle J, \\ \mathcal{H}_{ME}^{\alpha_2} &= -(D_{\alpha_2}^{\alpha_1}\epsilon^{\alpha_1} + D_{\alpha_2}^{\alpha_2}\epsilon^{\alpha_2}) (2 \langle J_z \rangle J_z - \langle J_x \rangle J_x - \langle J_y \rangle J_y)\end{aligned}\quad (3)$$

where $D_{\alpha_j}^{\alpha_i}$ are the two-ion magnetoelastic constants and ϵ^{α_i} are the normalized, symmetrized strains. ϵ^{α_1} is the volume strain while ϵ^{α_2} is the axial strain acting on the c/a ratio:

$$\begin{aligned}\epsilon^{\alpha_1} &= \frac{1}{\sqrt{3}}(\epsilon_{xx} + \epsilon_{yy} + \epsilon_{zz}) \\ \epsilon^{\alpha_2} &= \frac{1}{\sqrt{6}}(2\epsilon_{zz} - \epsilon_{xx} - \epsilon_{yy})\end{aligned}\quad (4)$$

The minimization of the free energy with respect to each strain yields the equilibrium values of, say, the α -strains:

$$\begin{aligned}\epsilon^{\alpha_1} &= M_{\alpha_1}^{\alpha_1} \langle J \rangle^2 + M_{\alpha_2}^{\alpha_1} (2 \langle J_z \rangle^2 - \langle J_x \rangle^2 - \langle J_y \rangle^2) \\ \epsilon^{\alpha_2} &= M_{\alpha_1}^{\alpha_2} \langle J \rangle^2 + M_{\alpha_2}^{\alpha_2} (2 \langle J_z \rangle^2 - \langle J_x \rangle^2 - \langle J_y \rangle^2)\end{aligned}\quad (5)$$

where $M_{\alpha_j}^{\alpha_i}$ ($i, j=1,2$) is a combinations of the $D_{\alpha_j}^{\alpha_i}$ and the symmetrized elastic constant $C_0^{\alpha_k}$ ($k=1,2,12$). The magnetoelastic couplings can be experimentally probed by measuring the macroscopic length change under an applied magnetic field. In a tetragonal symmetry, the relative length change, $\lambda = \frac{\partial l}{l}$, measured along the $(\beta_1, \beta_2, \beta_3)$ direction when an external field is along the (x, y, z) direction is given by:

$$\beta_1\beta_2\beta_3\lambda_{xyz} = \frac{1}{\sqrt{3}}\epsilon^{\alpha_1} + \frac{1}{\sqrt{6}}\epsilon^{\alpha_2}(2\beta_3^2 - \beta_1^2 - \beta_2^2) + \frac{1}{\sqrt{2}}\epsilon^\gamma(\beta_1^2 - \beta_2^2)\quad (6)$$

where ϵ^γ corresponds to the strain mode that leads to a symmetry lowering from tetragonal to orthorhombic. This ϵ^γ mode can be determined from the appropriate magnetostriction measurements, namely:

$$\epsilon^\gamma = \frac{1}{\sqrt{2}}({}^{100}\lambda_{100} - {}^{010}\lambda_{100}) \quad (7)$$

The thermal and field variation of the measurable magnetostrictions arise from the T - and H -dependence of $\langle J_i \rangle$. The calculation of such a dependence is usually carried out either by proper diagonalization of the total Hamiltonian (mostly appropriate for the ordered state and higher applied fields) or by perturbation methods (appropriate within the paramagnetic phase and for small magnetic fields). Here we will be concerned only with the paramagnetic case (for more details see Ref.¹⁹). Utilizing the susceptibility formalism¹⁹, one gets the following useful relations:

$$\begin{aligned} \epsilon^{\alpha_i} &= \chi_{100}^{\alpha_i} H^2 \\ \epsilon^{\alpha_i} &= \chi_{001}^{\alpha_i} H^2 \end{aligned} \quad (8)$$

where $\chi_j^{\alpha_i}$ ($i=1,2$) is the strain field susceptibility along the indicated direction. A complete description of the parastriction can be obtained by combining these equations and Eqs.5 together with the relation:

$$\langle J_i \rangle = \frac{\chi_i}{N_A g \mu_B} H; \quad i = x, y, z; \quad N_A \text{ is the Avogadro number} \quad (9)$$

III. EXPERIMENTAL

Single crystals were grown by floating zone method.²⁰ X-ray and magnetic measurements revealed a single phase of an excellent quality. The size and orientation of the rectangular spark-cut bars were chosen to suit the requirement of the magnetization or the magnetostriction measurements. The isofield and isothermal magnetization curves were measured by the extraction method for temperatures down to 1.5 K and fields up to 160 kOe. The sensitivity of the measurement is better than 5×10^{-5} emu.

The magnetostriction measurement were performed using a high-accuracy capacitance dilatometer which allows for measuring thermal expansion and forced magnetostriction in the temperature range of 3 - 250 K and under magnetic field up to 65 kOe. The typical resolution is better than 1 Å. In addition, the set-up allows for the rotation of the capacitance cell around the vertical axis of the cryostat while the field is maintained in a horizontal direction. In this way, the angle between the sample axis and the field direction can be varied across the range 0 – 180°. The relative length variation for temperature scan at fixed fields is defined as $\lambda_H = [l(T) - l(T_0)] / l(T_0)$ while that for field scan at fixed temperatures is defined as $\lambda_T = [l(H) - l(H = 0)] / l(H = 0)$. Diamagnetic contributions and demagnetizing fields are expected to be small and as such no correction for their influences on the magnetization or magnetostriction curves were attempted.

IV. RESULTS AND ANALYSIS

Below we show representative magnetization and magnetostriction curves taken within the paramagnetic and the ordered phase. By applying the field along the (001) or (100) direction, it was possible to investigate separately the volume distortion ϵ^{α_1} , the axial distortion ϵ^{α_2} or the orthorhombic distortion ϵ^γ . The paramagnetic and parastriction curves were analyzed according to susceptibility formalism given in Sec.II. Based on the overall analysis of the ordered state, $H - T$ phase diagrams for $H // (100)$ and $H // (001)$ are constructed.

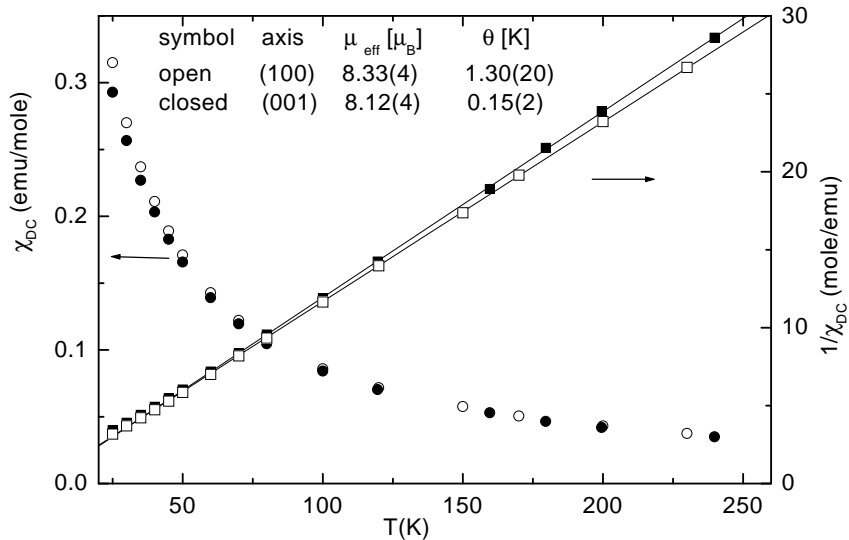


Fig-1

FIG. 1: Thermal evolution of the paramagnetic susceptibilities (circles) and their reciprocals (squares). The open and closed symbols represent, respectively, measurements along the a-axis and the c-axis. Each point was obtained from an Arrott plot (M^2 versus H/M). The effective moment and Curie-Weiss temperature for each orientation are given in the inset table.

A. Paramagnetic Phase

1. Magnetization

The paramagnetic susceptibilities were deduced at each temperature ($25 \text{ K} < T < 300 \text{ K}$) from the Arrott plot (M^2 versus H/M). The thermal evolution of these susceptibilities along each of the (100) and (001) direction (shown in Fig.1) reveals a weak anisotropic character, similar to the one reported by Canfield et al¹⁴. From the analysis of Fig.1 and according to Eq.2, we obtained $n^{\alpha_1} = 0.12(\pm 0.04)$ mole/emu and $n^{\alpha_2} = -0.05(\pm 0.04)$ mole/emu. The experimental error involved in the determination of these n^{α_1} and n^{α_2} were dictated by the experimental resolution, nonetheless, the determination of their signs and their magnitudes are consistent with the results of Canfield et al¹⁴: on the one hand, n^{α_1} is positive and weak indicative of a small effective θ . On the other hand, the magnitude of n^{α_2} is twice smaller (indicative of a weak paramagnetic anisotropy) and its sign is negative (i.e. $\chi_{\parallel c} < \chi_{\perp c}$) implying that it is energetically favorable for the spins to lie within the basal plane.

The effective moments deduced from the slope of the inverse susceptibilities were found to be $\mu_{\text{eff}[100]} = 8.33(4) \mu_B$ and $\mu_{\text{eff}[001]} = 8.12(4) \mu_B$; both are slightly higher than the theoretical value ($\mu_{\text{eff}} = 7.94 \mu_B$). Such a small discrepancy arises possibly due to matrix contribution: an exchange-enhancement of the Ni-sublattice susceptibility and/or a polarization of the conduction band.

Representative curves of the parastrictions $^{100}\lambda_{100}$, $^{010}\lambda_{100}$, and $^{001}\lambda_{100}$ are shown in Fig.2. Similar curves (not shown) were obtained as well for $^i\lambda_{010}$ and $^i\lambda_{001}$ ($i = (100), (010), (001)$). In all cases, λ is of the order of few 10^{-5} , explaining the earlier report that magnetoelastic effects were apparently absent in the temperature-dependent XRD measurements.²¹

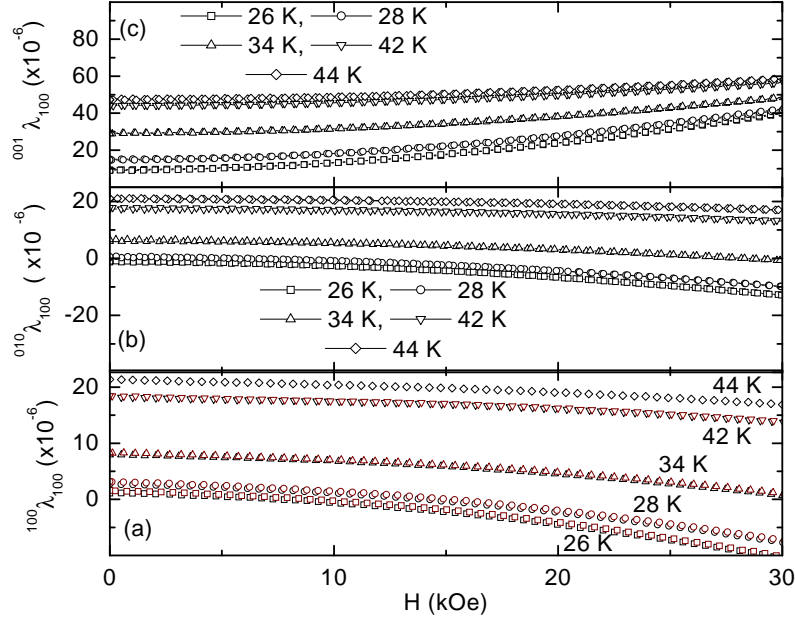


Fig.2

FIG. 2: Representative parastriction isotherms with the field along the a-axis. The relative length variation λ is measured along (a) the a-axis, (b) the b-axis, and (c) the c-axis.

Fig.3 shows the symmetrized, normalized strains $\epsilon^{\alpha 1}$ and $\epsilon^{\alpha 2}$ which were constructed from parastrictions curves (as those in Fig.2) according to Eq.6. Both $\epsilon^{\alpha 1}$ and $\epsilon^{\alpha 2}$ are nonzero and follow faithfully the quadratic field dependence (see Eq.8). These results coupled with the tetragonal character of $\text{GdNi}_2\text{B}_2\text{C}$ predict a magnetic contribution to the thermal expansion, in addition to the conventional contribution expected in the diamagnetic isomorph $R\text{Ni}_2\text{B}_2\text{C}$ ($R=\text{Lu}, \text{Y}, \text{La}$). The symmetry lowering mode ϵ^γ (not shown) is mostly field-independent ruling out any possibility for a field-induced orthorhombic distortion within the paramagnetic phase.

Fig.4 shows the thermal evolution of $\chi_{100}^{\alpha 1}(T)$ and $\chi_{001}^{\alpha 1}(T)$. These curves were obtained from the analysis of Fig.3 according to Eq.8. Following the same procedure, we obtained the $\chi_{100}^{\alpha 2}(T)$ and $\chi_{001}^{\alpha 2}(T)$ curves (shown in Fig.5). Within this paramagnetic range and according to Eqs.6 we get:-

$$\begin{aligned}\epsilon_{H//100}^{\alpha 1} &= \epsilon_{H//001}^{\alpha 1} \\ \epsilon_{H//100}^{\alpha 2} &= \epsilon_{H//001}^{\alpha 2}\end{aligned}\quad (10)$$

then:

$$\begin{aligned}\chi_{100}^{\alpha 1} &= \chi_{001}^{\alpha 1} \\ \chi_{100}^{\alpha 2} &= \chi_{001}^{\alpha 2}\end{aligned}\quad (11)$$

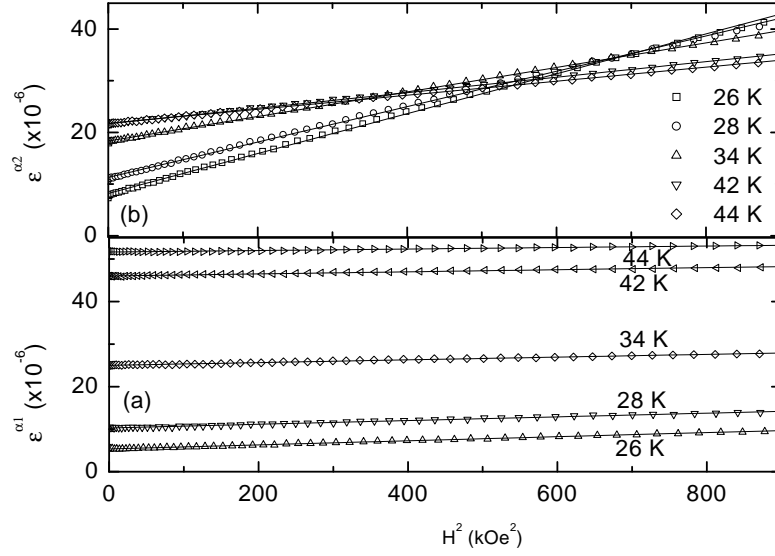


Fig.3

FIG. 3: The normalized symmetrized strains (see Eq.4) plotted against the square of the field (H/a). (a) $\epsilon^{\alpha 1}$ vs H^2 and (b) $\epsilon^{\alpha 2}$ vs H^2 . The continuous lines are the least-square fit of Eq.8 to the experimental points (symbols).

Within the experimental errors, these equalities were experimentally confirmed in Figs.4-5: the analysis of the $\chi^{\alpha 1}$ curves gave:

$$\begin{aligned} 1/\sqrt{\chi_{100}^{\alpha 1}(T)} &= 361(30) + 41(1)xT \\ 1/\sqrt{\chi_{001}^{\alpha 1}(T)} &= 324(73) + 36(2)xT \end{aligned} \quad (12)$$

while for the $\chi^{\alpha 2}$ curves gave:

$$\begin{aligned} 1/\sqrt{\chi_{100}^{\alpha 2}(T)} &= -27(17) + 20(1)xT \\ 1/\sqrt{\chi_{001}^{\alpha 2}(T)} &= -37(26) + 21(1)xT \end{aligned} \quad (13)$$

Thus, the thermal evolutions of the two α_1 - curves (as well the α_2 -curves) are similar: the small numerical discrepancy is attributed to artefacts stemming from the very small values of $\chi^{\alpha i}$ ($i = 1, 2$).

From these expressions and the above-cited equations, $M_{\alpha j}^{\alpha i}$ ($i, j=1,2$) can be straightforwardly calculated. However since the values of the symmetrized elastic constant $C_0^{\alpha k}$ ($k=1,2,12$) are unavailable, these calculation are not sufficient for determining the extremely useful magnetoelastic constants $D_{\alpha j}^{\alpha i}$.

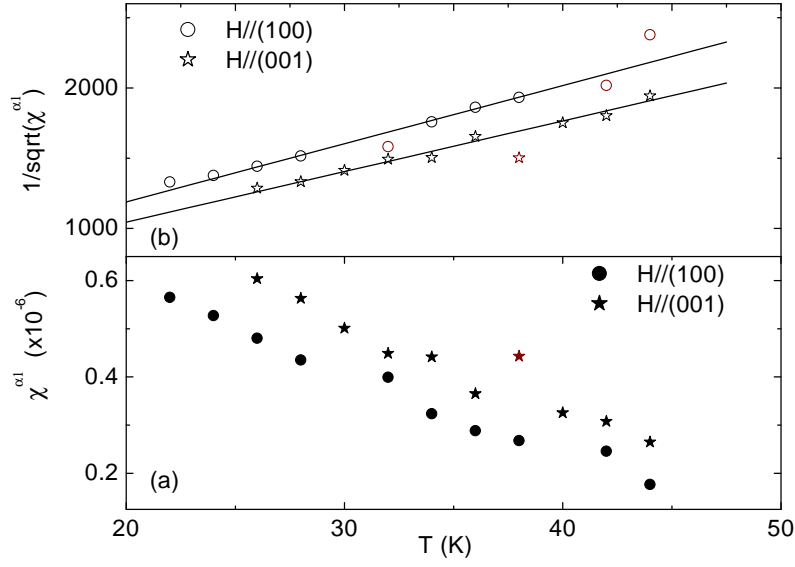


Fig.4

FIG. 4: The thermal variation of the strain susceptibilities (a) $\chi_{100}^{\alpha_1}(T)$, $\chi_{001}^{\alpha_1}(T)$ and (b) $\sqrt{1/\chi_{100}^{\alpha_1}(T)}$ and $\sqrt{1/\chi_{001}^{\alpha_1}(T)}$. The continuous lines are least-square fitting of the experimental points (symbols).

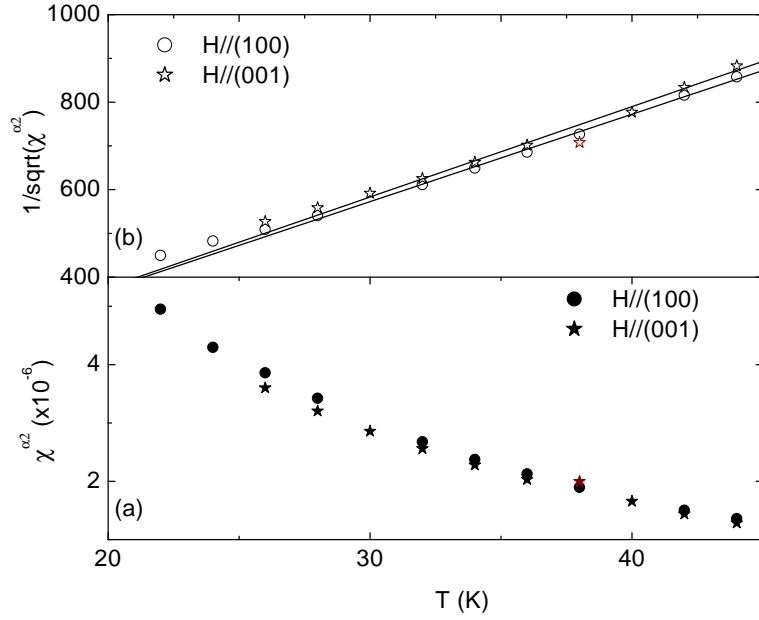


Fig.5

FIG. 5: The thermal variation of the strain susceptibilities (a) $\chi_{100}^{\alpha_2}(T)$, $\chi_{001}^{\alpha_2}(T)$ and (b) $\sqrt{1/\chi_{100}^{\alpha_2}(T)}$ and $\sqrt{1/\chi_{001}^{\alpha_2}(T)}$. The continuous lines are least-square fitting of the experimental points (symbols).

B. The Ordered Phase

1. Magnetization

Fig.6a shows representative magnetization isotherms along the a-axis, M_{100} . Each $M_{100}(H)$ isotherm increases monotonically with the field and, for a certain field range, such an increase is linear. Moreover, for low temperatures, $M_{100}(H)$ curves demonstrate a weak event at $H_D \approx 12$ kOe (defined as the field value at which $(\partial M/\partial H)_T$ is a maximum) and, on a further field increase, a saturation at a relatively high field, for instance $H_S(1.5 \text{ K}) = 128$ kOe. It was observed that on increasing the temperature, the saturation process becomes less pronounced. The thermal evolution of each of H_D and H_S were plotted in Fig.11. The saturated moment ($7.2\mu_B$ at $T = 1.5\text{K}$) is weakly enhanced in comparison with the theoretically expected value ($7\mu_B$). This enhancement is attributed to matrix contribution, just as the above-mentioned enhancement of the effective moment.

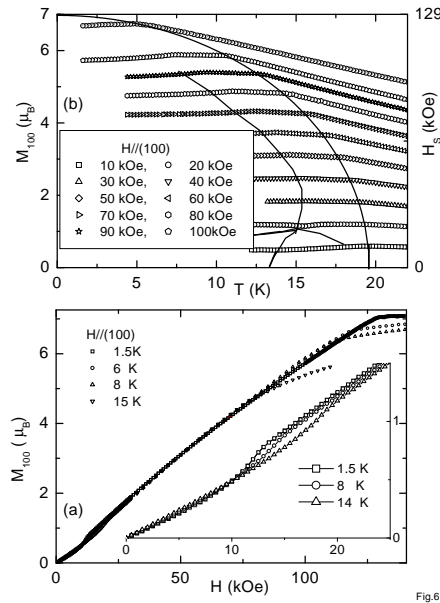


FIG. 6: (a) Representative low-temperature magnetization isotherms along the a-axis (M_{100}). The inset shows an expanded view of the low-field part of the magnetization isotherm. (b) The thermal variation of the magnetization for representative magnetic field ($H//a$). The continuous lines in Fig.6b represent the thermal evolution of H_D , H_R , and H_S as determined from the analysis of Figs.6a,8-10b.

The thermal variation of the isofield $M_{100}(T)$ is shown in Fig.6b. Characteristic features signaling magnetic events at H_D and H_S were also observed and their values were found to agree with the values obtained from the magnetization isotherms of Fig.6a. This agreement was convincingly demonstrated by plotting in Fig.6b the thermal evolution of each of H_D and H_S . Moreover, Fig.6b shows an extra curve, H_R , representing the spin reorientation process (see below).

Representative magnetization isotherms along the c-axis (M_{001}) are shown in Fig.7. These isotherms are very similar to the M_{100} ones except that (i) there are only two events namely at H_R and H_S , (ii) the field dependence of the magnetization at these events is more pronounced, and (iii) H_R was observed to have a different temperature dependence than the corresponding one along

the a -axis. However, for both orientation, the saturation is reached at the same $H_S(T)$ curve. The thermal evolution of H_S and H_R deduced from Fig.7 were plotted in Fig.12. It is worth noting that within the experimental conditions of the extraction technique, no hysteresis features or relaxation effects were observed.

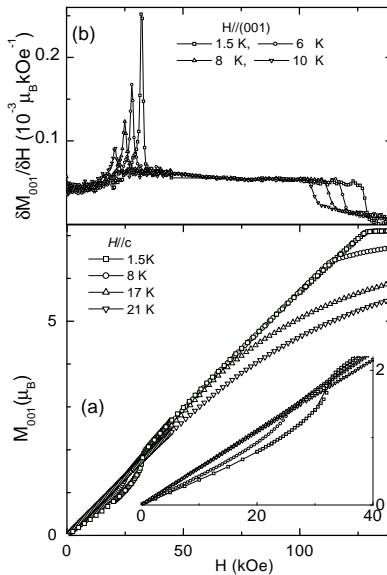


Fig.7

FIG. 7: (a) Representative low-temperature magnetization isotherms along the c -axis (M_{001}). The inset shows an expanded view of the low-field part of selected magnetization isotherms. (b) Field derivatives of magnetization isotherms showing the onset of $H_R(T)$ (the field at which the maximum is attained) and $H_S(T)$ (the field of maximum inclination).

2. Magnetostriction

Fig.8a shows the forced magnetostriction curves, $^{100}\lambda_{100}(H)$, at various temperatures. For lower temperatures, a field increase is accompanied by a steep increase in $^{100}\lambda_{100}$, then a shallow maximum, and afterwards a steady decrease with a weak slope. The initial steep increase is very likely to be due to the domain-purifying influence of the applied field: the field derivative of λ shows a maximum at H_D (compare Fig.6a with Fig.8b). Surprisingly the $^{100}\lambda_{100}$ curves present a very small hysteresis suggesting that the domain distribution has a weak dependence on the sample history.

The thermal evolution of the isofield $^{100}\lambda_{100}(T)$ (shown in Fig.9) manifests magnetic events that are very much similar (though more pronounced) to the ones observed in the magnetization (Figs.6b) and forced magnetostriction curves (Fig.8.a). The corresponding field and temperature values at these events were plotted in Fig.11.

It is interesting to note that for intermediate fields, e.g. $H = 15$ kOe in Fig.9, on decreasing the temperature below T_N , $^{100}\lambda_{100}(T)$ shows at first a slow increase till 17.4 K where a decrease commences and continues till T_R . Afterwards $^{100}\lambda_{100}(T)$ increases fast but later tends to saturate to 1.3×10^{-4} at $T = 0$ K. In contrast, for lower (higher) fields, $^{100}\lambda_{100}(T)$ is monotonically decreasing

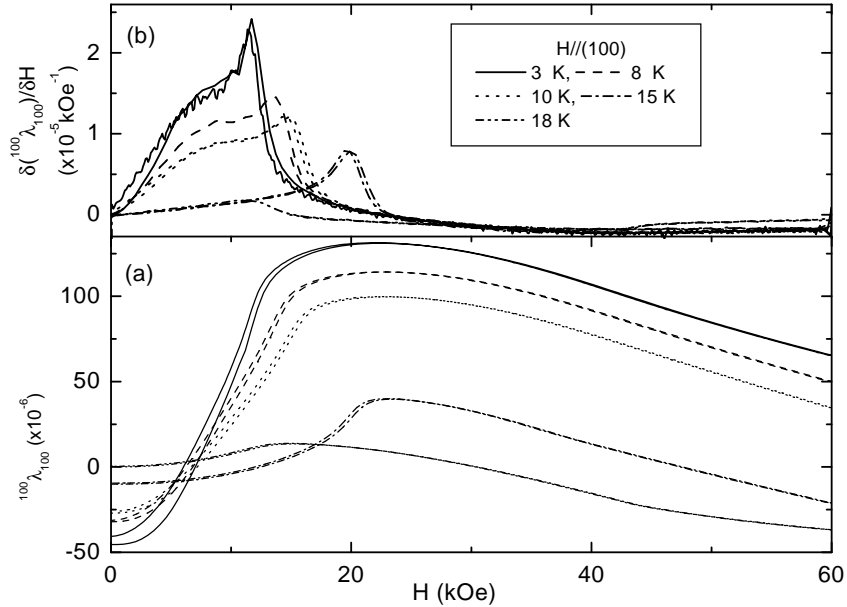


Fig.8

FIG. 8: (a) Representative forced magnetostriction curves at various temperatures. Measurements were taken while increasing and decreasing the field. (b) Field derivative of these magnetostriction isotherms. Note that in (b) the shoulder at the left hand side of $H_D(T)$ disappears when the temperature is increased above $T_R(H=0)$ suggesting a correlation between this shoulder and the reorientation process below $T_R(H)$.

(increasing) with decreasing temperature, tending to saturate at $T=0$ K. For all applied fields, the signature of the event at $T_R(H)$ is clearly observable but tends to fade away as higher fields are approached. It is also interesting to compare the magnitude of this two-ion effect with the one observed in typical single-ion compound such as $\text{ErNi}_2\text{B}_2\text{C}$ (Ref.¹⁰): for zero field, the saturation value of $^{100}\lambda_{100}$ in $\text{GdNi}_2\text{B}_2\text{C}$ is $\sim -0.5 \times 10^{-4}$ while in $\text{ErNi}_2\text{B}_2\text{C}$ is $\sim -3 \times 10^{-4}$.

Fig.10a shows an impressive demonstration of the magnetic domain effects within the ordered state. In these curves, the angular dependence of various $^{100}\lambda_\theta$ isotherms was monitored by rotating the single crystal in a field of, say, 30 kOe. Furthermore, Fig.10b shows the orthorhombic strain ϵ^γ for $H=7.5, 30$ kOe, constructed according to Eq.7. Under $H=30$ kOe and a decreasing temperature below T_N , ϵ^γ commences to increase slowly till $T_R(=15.5$ K) and afterwards with a faster rate till reaching saturation of -2.6×10^{-4} . Across the borocarbides, this two-ion orthorhombic distortion should vary roughly with the de Gennes factor and as such for $\text{ErNi}_2\text{B}_2\text{C}$ this partial contribution amounts to $\epsilon^\gamma \approx -0.4 \times 10^{-4}$ which is one third of the total $\epsilon^\gamma \approx -1.4 \times 10^{-4}$ observed for $\text{ErNi}_2\text{B}_2\text{C}$ at 2.5 K (Ref.¹⁰): thus for borocarbides, the two-ion magnetoelastic contribution (in particular ϵ^γ) is not negligible as compared to that of the single-ion effect.

3. The $H - T$ Phase Diagram

Based on the analysis of the magnetization and magnetostriction curves, we were able to construct the $H - T$ phase diagrams with the field either along the a-axis (shown in Fig.11) or along the c-axis (shown in Fig.12). In both diagrams, the boundary describing the saturation process (when the exchange field is completely counterbalanced) is well described by the rela-

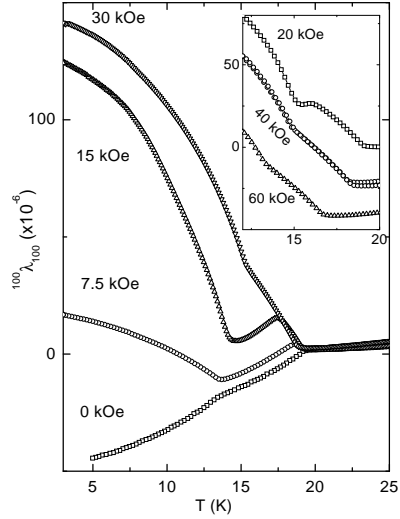


FIG. 9: Representative thermal evolution of the magnetostriction for various fields. Both the field and the length-measurement were oriented along the a-axis. The inset shows, in an expanded scale, the thermal evolution of the magnetostriction in the neighborhood of $T_R(H)$ and $T_N(H)$.

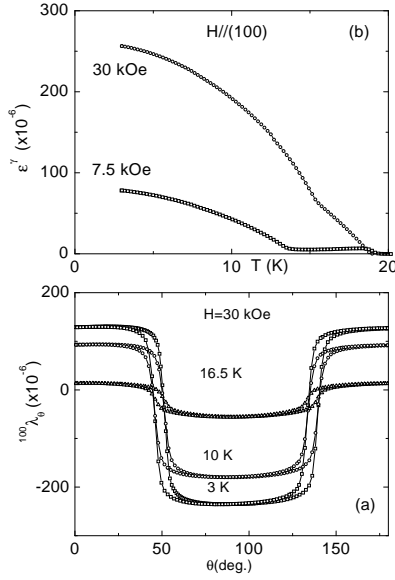


FIG. 10: (a) Angular dependence of $^{100}\lambda_\theta$ isotherms under $H = 30$ kOe and for $T = 3$ K, 10 K (below $T_R(H)$) and 16.5 K (above $T_R(H)$). (b) the thermal evolution of ϵ^γ taken at $H = 7.5$ kOe (below $H_R(T < 13.5$ K)) and at $H = 30$ kOe (above $H_R(T < 13.5$ K)).

tion $H_S \left[1 - (T/T_N)^2\right]^{\frac{1}{2}}$ kOe with $H_S(T \rightarrow 0)=128.5(5)$ kOe and $T_N(H \rightarrow 0)=19.5$ K. The second boundary, denoted by $H_R(T)$, is attributed to the reorientation process: its evolution for $H//c$ (much simpler than that for $H//a$) is given by the relation $H_R(1-T/T_R)^{\frac{1}{3}}$ kOe where $H_R(T \rightarrow 0)=33.5(5)$ kOe and $T_R(H \rightarrow 0)=13.5$ K. The extrapolated values of the characteristic points H_S, T_N, T_R are in excellent agreement with the reported ones.^{8,14,16,17,18} The third boundary $H_D(T)$, appearing only in the a-axis phase diagram, (see Fig.11) is related to the domain effects as can be inferred from the angular dependence of Fig.10.a. This $H_D(T)$ has the following features: (i) the extrapolated $H_D(T \rightarrow 0)=12.0(5)$ kOe while $T_D(H \rightarrow 0) = T_N(H \rightarrow 0) = 19.5$ K, (ii) it is almost constant for $T < 8$ K, increases slowly up to a maximum around 16 K and afterwards decreases steadily till vanishes at T_N : such an increase of H_D with temperature is not usual for domain effects.

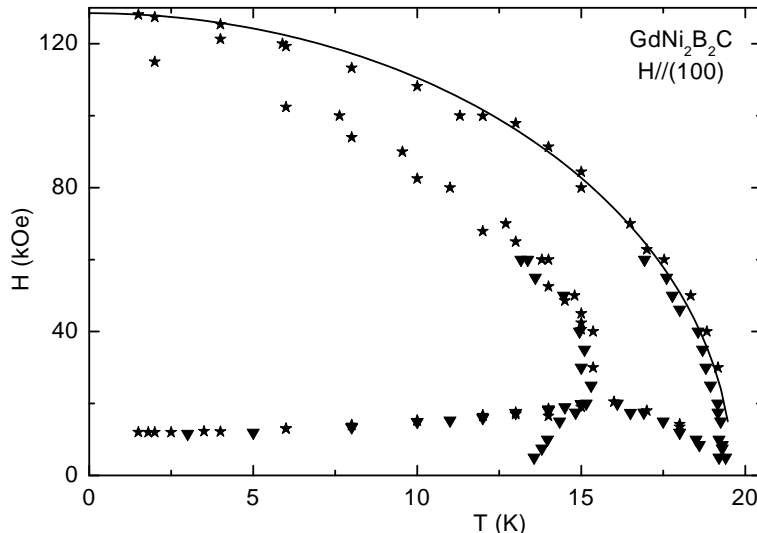


Fig.11

FIG. 11: The $H - T$ phase diagram along the a-axis as compiled from the magnetization (\star) and magnetostriction (\blacktriangledown) measurements. The continuous line represents the best fit of the experimental points to $H_S(1-(T/T_N)^2)^{\frac{1}{2}}$ kOe where H_S and T_N were found, respectively, to be 128.5(5) kOe and 19.5 K.

V. DISCUSSION

The modulated state in $\text{GdNi}_2\text{B}_2\text{C}$ (and borocarbides in general) is usually related to the nesting features in their electronics structures.²² Below, we discuss the stability of this state against field and temperature variation. First MFA arguments are applied to account for H_S , H_D , and the linearity of the magnetization isotherms. Next, anisotropic perturbations are introduced and afterwards the anisotropic exchange interaction and magnetoelastic couplings are considered.

Among the borocarbides, $\text{GdNi}_2\text{B}_2\text{C}$ has the strongest exchange interactions and the weakest magnetic anisotropy. The strength of the exchange interactions (denoted as H_{ex} , or J_{eff}) is reflected as a high value of T_N and H_S (see Figs.11-12) while the weakness of the magnetic anisotropy

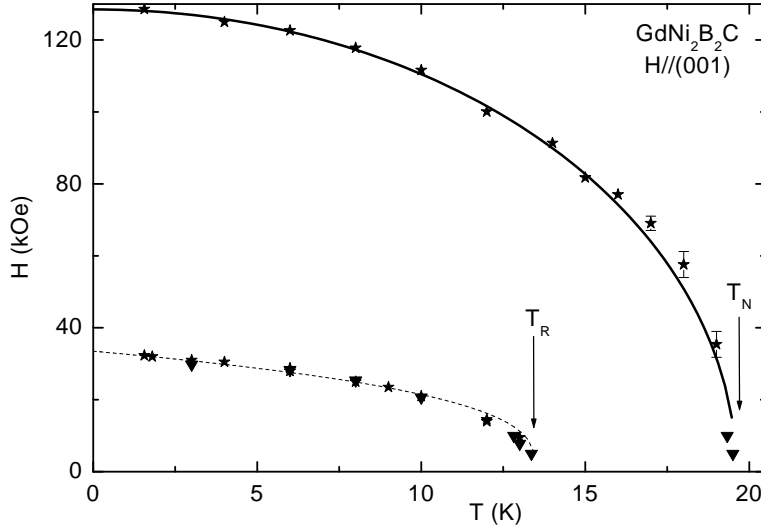


Fig.12

FIG. 12: The $H-T$ phase diagram ($H//001$) as compiled from the magnetization (\star) and magnetostriction (\blacktriangledown) curves. The continuous line represent the best fit of the data to $H_S \left[1 - (T/T_N)^2\right]^{\frac{1}{2}}$ kOe with $H_S(T \rightarrow 0)=128.5(5)$ kOe and $T_N(H \rightarrow 0)=19.5$ K. The dashed lines represent the best fit to $H_R(1-T/T_R)^{\frac{1}{3}}$ kOe where $H_R(T \rightarrow 0)=33.5(5)$ kOe and $T_R(H \rightarrow 0)=13.5$ K.

(denoted as H_{an}) is manifested as low H_D and as a weak difference between the parallel and perpendicular paramagnetic susceptibility. MFA arguments can be used to calculate an effective value for each of H_{ex} , J_{eff} , and H_{an} from the observed values of T_N , H_S , and H_D . Let us, at first, ignore the anisotropic feature ($H_{an}=0$). Then, from the relation $zJ_{eff} = \frac{3T_N}{2S(S+1)}$ (z is an effective nearest neighbors), zJ_{eff} was calculated ≈ 1.86 K. Substitution of this value into the relation $H_S = 2zJ_{eff}S(S+1)/g\mu_B S$ gave $H_S \approx 125$ kOe, a reasonable value for the effective saturation field. Next, taking into account the case $H_{an} \neq 0$ and using Eqs.14, one is able to calculate an effective value for each of H_{ex} and H_{an} and furthermore to account for the observed linearity of $M_{100}(H_D < H < H_S)$:²³

$$\begin{aligned}
 H_S &= (H_{ex} - H_{an}) \\
 H_D &= \sqrt{H_{an}H_{ex} - H_{an}^2} \\
 \langle M_{100} \rangle / M_s &= H/H_S, \text{ for } H_D < H < H_S
 \end{aligned}
 \tag{14}$$

Substituting the extrapolated $H_S(T \rightarrow 0 \text{ K})$ and $H_D(T \rightarrow 0 \text{ K})$ (see Fig.11 below) one obtains the satisfactory value $H_{ex}(T \rightarrow 0 \text{ K}) = 129.6(5)$ kOe and $H_{an}(T \rightarrow 0 \text{ K})=1.1(3)$ kOe: as expected for a Gd-based compound, the former is much stronger than the latter.

In the above treatment, the zero-temperature magnetic structure is implicitly assumed as a collinear 3d AF state. Rather, for $T_R(H=0) < T < T_N$, the magnetic structure is a modulated state with no c-component and the ordered moments are distributed among the a- or b-polarized domains. Then applying a field along the a-axis would force the a-polarized domains to align perpendicular to the field at $H_D(T > T_R)$ and later on to achieve saturation at $H_S(T > T_R)$. For the same temperature range, a field applied along the c-axis is already perpendicular to the domains

and as such only the saturation transition would appear. On the other hand for $T < T_R(H = 0)$, the spontaneous emergence of the c-component at $H_R(T)$ constitutes an extra event for both field orientations: thus for $H//a$ -axis, there are three transitions (at H_D , H_R , and H_S) while for the $H//c$ -axis, there are only two transitions (at H_R and H_S).

Within the ordered phase, the manifestation of the magnetoelastic coupling and anisotropic exchange interactions is much more pronounced, leading to a substantial perturbation of the nuclear and the magnetic structures. To demonstrate the importance of these perturbations, let us divide the ordered phase into two regions depending on the magnitude of ϵ^γ . The first region is $T_R < T < T_N$ wherein the low-field ϵ^γ is relatively weak (see Fig.10) and as such is hardly sufficient to modify (substantially) the nuclear structure or the modulated magnetic state. The second region is $T < T_R$ wherein the magnitude of the low-field ϵ^γ is very large (see Fig.10) and increases whenever the temperature is decreased or the field is increased. As a consequence, the nuclear structure is distorted ($\frac{a}{b} < 1$ and the four-fold symmetry of the basal plane is reduced to a two-fold symmetry). In addition, there is an accompanying dramatic modification of the magnetic structure: as the temperature is decreased, the anisotropic character of the exchange interactions (just as the magnitude of ϵ^γ) is enhanced and the magnetic structure is more and more perturbed towards a squared-up state wherein the magnetic moments approach equal amplitudes and progressively bunch towards an orientation within the b-c plane. While the square-up character can be understood based on entropy arguments, the bunching of the moments is most probably induced by the above mentioned perturbations.

By demonstrating the presence of magnetoelastic and anisotropic exchange couplings in the ordered phase of $\text{GdNi}_2\text{B}_2\text{C}$, this work confirms the far-sight analysis of Detlefs et al⁸ and Tomala et al¹⁸. On the one hand, Detlefs et al attributed the strong asymmetry in the line shape of the resonant XRES below $T_R(H = 0)$ as being due to a straining. Consequently, their XRES spectra were analyzed as being composed of two peaks (thus the asymmetric character) below $T_R(H = 0)$ and as a single line above $T_R(H = 0)$. It is assuring to note that the thermal evolution of the position and intensity of these XRES peaks correlate very well with ϵ^γ (compare Fig.7 of Ref.⁸ with our Fig.10). Tomala et al, on the other hand, analyzed their ¹⁵⁵Gd Mossbauer spectra assuming a transverse (moments along b-axis) sine-modulated state above $T_R(H = 0)$ and a strongly *squared-up* and *bunched* state below $T_R(H = 0)$.

VI. CONCLUSION

We presented experimental results on single crystal of $\text{GdNi}_2\text{B}_2\text{C}$. The parastriction and paramagnetic features, well accounted for within the susceptibility formalism, demonstrated the presence of weak anisotropic exchange couplings and two-ion ϵ^{α_1} and ϵ^{α_2} strain modes. The strength of the latter coefficients indicate that the strain derivative of the coupling constant at the Brillouin zone centre have significant amplitudes. The ordered state, on the other hand, is characterized by very rich field and temperature phase diagrams that manifest high values of T_N and H_S (indicative of strong exchange interactions), a spin reorientation process at $H_R(T)$, and a domain-purifying field H_D . Anisotropic exchange interactions and relatively strong magnetoelastic couplings (particularly the orthorhombic distortion mode) were observed, lending support to the reported modification of the magnetic structure below T_R .

It is worth recalling that the modulated state of $\text{GdNi}_2\text{B}_2\text{C}$ within the temperature range $T_R < T < T_N$ is very much similar to that of $\text{ErNi}_2\text{B}_2\text{C}$ within the range $2 \text{ K} < T < T_N$, even though the dominant aligning forces operating in each isomorphs are very much different. Since the exchange interaction and the magnetoelastic couplings are driven by the indirect RKKY couplings and that de Gennes scaling holds well among the heavy borocarbides,²⁴ then both the anisotropy

exchange interactions and magnetoelastic couplings must be present (though with varying strength depending on de Gennes factor) in other borocarbide magnets. As such, these perturbations must be explicitly considered when discussing the magnetic properties (in particular the $H - T$ phase diagrams) of these magnets.

Acknowledgement 1 *M. ElM. acknowledge partial financial support from the Japan Society for the promotion of science, the University of Joseph Fourier of Grenoble, and the Brazilian agencies CNPq and FAPERJ.*

-
- ¹ J.W. Lynn, S. Skanthakumar, Q. Huang, S. K. Sinha, Z. Hossain, L.C. Gupta, R. Nagarajan, C. Godart, Phys. Rev. B **55**, 6584 (1997).
 - ² P. C. Canfield, S. L. Bud'ko, and B. K. Cho, Physica C **262**, 249 (1996); S. L. Bud'ko and P. C. Canfield, Phys. Rev. B **61**, R14 932 (2000); A. J. Campbell, D. McK. Paul and G. J. MacIntyre, Solid State Com **115**, 213 (2000).
 - ³ C. Detlefs, F. Bourdarot, P. Burlet, P. Dervenagas, S. L. Bud'ko and P. C. Canfield, Phys. Rev. B **61**, R14916 (2000); P. C. Canfield, S. L. Bud'ko, B. K. Cho, A. Lacerda, D. Farrell, E. Johnston-Halperin, V. A. Kalatsky, and V. L. Pokrovsky, Phys. Rev. B **55**, 970 (1997); A. J. Campbell, D. McK.Paul and G. J. McIntyre, Phys. Rev. B **61**, 5872 (2000).
 - ⁴ P.C. Canfield and S.L. Bud'ko, J. Alloys Compd. **262-263**, 169 (1997).
 - ⁵ P. Dervenagas, J. Zarestky, C. Stassis, A. I. Goldman, P. C. Canfield, and B. K. Cho, Physica B **212**, 1 (1995).
 - ⁶ P. Dervenagas, J. Zarestky, C. Stassis, A. I. Goldman, P. C. Canfield, and B. K. Cho, Phys. Rev. B **53**, 8506 (1996); B. K. Cho, P. C. Canfield, and D. C. Johnston, Phys. Rev. B **53**, 8499 (1996).
 - ⁷ J. Zarestky, C. Stassis, A. I. Goldman, P. C. Canfield, P. Dervenagas, B. K. Cho, and D. C. Johnston, Phys. Rev. B **51**, 678 (1995); S. K. Sinha, J. W. Lynn, T. E. Grigereit, Z. Hossain, L. C. Gupta, R. Nagarajan, and C. Godart, Phys. Rev. B **51**, 681 (1995).
 - ⁸ C. Detlefs, A. I. Goldman, C. Stassis, P. C. Canfield, B. K. Cho, J.P. Hill, and D. Gibbs, Phys. Rev. B **53**, 6355 (1996).
 - ⁹ A. Amici and P. Thalmeier, Phys. Rev. B **57**, 10684 (1998); V. A. Kalatsky and V. L. Pokrovsky, Phys. Rev. B **57**, 5485 (1998).
 - ¹⁰ M. Doerr, M. Rotter, M. El Massalami, S. Sinning, H. Takeya and M. Loewenhaupt, J. Phys: Cond. Matter **14** 5609 (2002)..
 - ¹¹ A. Kreyssig, M. Loewenhaupt, J. Freudenberger, K.-H. Muller, and C. Ritter, J. Appl. Phys, **85**, 6058 (1999); G. Oomi, T. Kagayama, H. Mitamura, T. Goto, B. K. Cho, P. C. Canfield, Physica B 294-295, 229 (2001).
 - ¹² C. Sierks, M. Doerr, A. Kreyssig, M. Loewenhaupt, Z. Q. Peng, K. Winzer, J. Mag. Mag. Mat. **192**, 473 (1999).
 - ¹³ C. Song, J. C. Lang, C. Detlefs, A. Letoublon, W. Good, J. Kim, D. Wermeille, S. L. Budko, P. C. Canfield, A. I. Goldman, Phys. Rev. B **64**, 020403 (2001); C. Song, D. Wermeille, A. I. Goldman, P. C. Canfield, J. Y. Rhee and B. N. Harmon, Phys. Rev B **63**, 104507 (2001).
 - ¹⁴ P. C. Canfield, B. K. Cho, K. W. Dennis, Physica B **215**, 337 (1995).
 - ¹⁵ T. Siegrist, H.W. Zandbergen, R.J. Cava, J.J. Krajewski and W. F.Peck, Nature **367**, 254 (1994); T. Siegrist, R.J. Cava, J.J. Krajewski and W. F.Peck, Jr, J. Alloys Compd. **216**, 135 (1994).
 - ¹⁶ M. El Massalami, B Giordanengo, J. Mondragon, E. M. Baggio-Saitovitch, A. Takeuchi, J. Voiron and A. Sulpice, J. Phys:Condens Matter **50**, 10015 (1995); M. El Massalami, S.L. Bud'ko, B. Giordanengo, M.B. Fontes, J.C. Mondragon and E. M. Baggio-Saitovitch, Phys. Status Solidi B **5**, 489 (1995).
 - ¹⁷ C. Godart, I. Felner, H. Michor, G. Hilscher, E. Tominez, E. Alleno, J. Alloys Compd. **277**, 642 (1998).
 - ¹⁸ K. Tomala, J. P. Sanchez, P. Vulliet, P. C. Canfield, Z. Drzazga, A. Winiarska, Phys. Rev. B **58**, 8534 (1998); D. R. Sanchez, H. Micklitz, M. B. Fontes, et al., J. Phys: Condens Matter, **9**, L299-L302 (1997); F.M. Mulder, J. V. V. J. Brabers, R. Cochoorn, R.C. Thiel, K. H. J. Buschow, F. R.de Boer, J. Alloys Compd. **217**, 118 (1995).

- ¹⁹ P. Morin, J. Rouchy, and D. Schmitt, Phys. Rev. B **37**, 5401 (1988).
- ²⁰ H. Takeya, T. Hirano, K. Kadowaki, Physica C **256**, 220 (1996).
- ²¹ A. Lindbaum and M. Rotter, preprint submitted to Elsevier (2002).
- ²² J.Y. Rhee, X. Wang, and B. N. Harmon, Phys. Rev.B **51**, 15 585 (1995).
- ²³ J.S. Smart, *Effective Field Theories of Magnetism*, (W.B.Saunders Company,1966) p.101; J.S. Smart, in "Magnetism.III", ed. G.Rado and H. Suhl, (Academic Press, London, N.Y., 1963) p.63.
- ²⁴ P. C. Canfield, O. L. Gammel, and D. J. Bishop, Phys. Today, **51**, 40 (1998).